

Multi-objective Design and Benchmark of Wide Voltage Range Phase-Shift Full Bridge DC/DC Converters for EV Charging Application

Dingsihao Lyu, *Member, IEEE*, Thiago Batista Soeiro, *Senior Member, IEEE*,
Pavol Bauer, *Senior Member, IEEE*

Abstract—This paper presents an analysis, multi-objective design, and benchmark of three modified Phase-Shift Full-Bridge (PSFB) converters that are well-suited for Electric Vehicle (EV) battery charging applications, covering both typical battery voltage classes (400V and 800V). These three modified PSFB converters, denoted as the t-PSFB, r-PSFB, and i-PSFB converters, have the ability to reconfigure and provide better efficiency performance in the wide voltage range necessary for public EV battery charging applications. In this paper, the characteristics and design considerations of these reconfigurable PSFB converters are discussed in detail. A multi-objective converter design process is proposed to optimize the average efficiency, normalized cost, and power density of the magnetic components and heat sinks. This design process employs the correlations between the cost and performance indexes of the key components derived based on open and accessible components data to estimate the design objectives. In this way, the design process is not constrained by certain component choices, making it easier to identify the most advantageous design. A benchmark study is conducted among the re-configurable PSFB topologies and the conventional PSFB circuit using the proposed multi-objective design process. To validate the analysis, a close-to-Pareto-front 11kW, 45kHz r-PSFB converter prototype with 640-840V input voltage and 250-1000V output voltage ranges is developed and tested.

Index Terms—phase shift full bridge, DC/DC converter, EV charging, wide voltage range, reconfiguration

I. INTRODUCTION

THE Phase-Shift Full-Bridge (PSFB) isolated DC/DC converter shown in Figure 1(a) is a popular circuit in the application of Electric Vehicle (EV) charging, notably because this circuit features a current source behavior which facilitates the start-up and the control of the battery charging profile. Additionally, this circuit technology is mature, power efficient, simple to operate, and well-established in several other applications [1]–[12]. Unfortunately, the conventional PSFB (or conv-PSFB) topology is challenged to keep the high efficiency within an extensive output voltage range. The reason is that the efficiency of the PSFB technology drops as the phase-shift angle increases (or equivalent duty cycle and consequently the output voltage decreases).

Most EVs launched last decade have a nominal battery voltage of around 400V. As of today, the component technology for this voltage class is well-established with several automotive-qualified components available. Currently, the manufacturers of high-end EVs are moving toward the 800V battery architectures [13]–[16] because the higher voltage

results in weight saving across the EV and the potential reduction of the battery charging time while using a public DC-fast charging infrastructures, i.e., as the current rating of the public charger cables are limited to 350A the high voltage will potentially enable higher power injection into the battery bank where the limits will be imposed by the public charger and the thermal management of the battery. Therefore, today the public DC-type EV charging infrastructures should be able to supply power efficiently to both 400V and 800V EV battery classes.

Studies have been conducted to extend the PSFB-type converter's voltage range while keeping high efficiency. The work developed in [3] proposes a hybrid-switching PSFB converter that provides for the H-bridge converter a wide Zero Voltage Switching (ZVS) range for the leading leg and Zero Current Switching (ZCS) for the lagging leg. Interestingly, the freewheeling circulating losses can also be improved, and the undesirable voltage overshoots at the rectifying stage can be clamped well. However, additional passive components (two diodes, a capacitor, and an inductor) are needed, and the complexity of the converter increases. The work in [4] proposes a secondary-side PSFB converter that extends the soft-switching operation and improves the circulating current losses, but it comes with the cost of two additional switches and complex control. In [9], a ZVS full-bridge DC/DC converter is proposed, incorporating a diode clamping circuitry on the primary side for the voltage ringing clamping and uses an asymmetrical PWM modulation together with an additional auxiliary inductor to reduce circulating current losses. Unfortunately, none of these studies have investigated and proved with experimental results the high-efficiency performance in the voltage range of 400V and 800V EV charging.

Based on the idea of a re-configurable PSFB converter [17]–[20], the study in [12] provides a solution for the extensive voltage range necessary in today's market of public EV charging stations (e.g., 250-1000V). This circuit, denoted here as the r-PSFB converter, employs a two-secondary-winding transformer, two diode rectifiers, and three auxiliary switches as shown in Figure 1(b). By controlling the connection of the auxiliary switches, the two secondary sides can be connected in series when the required output voltage is high or in parallel when the needed output voltage is low. As a result, rectifier diodes with a halved voltage rating and transistors with a halved current rating can be utilized. Most importantly, the range of the phase shift control angle needed for the wide

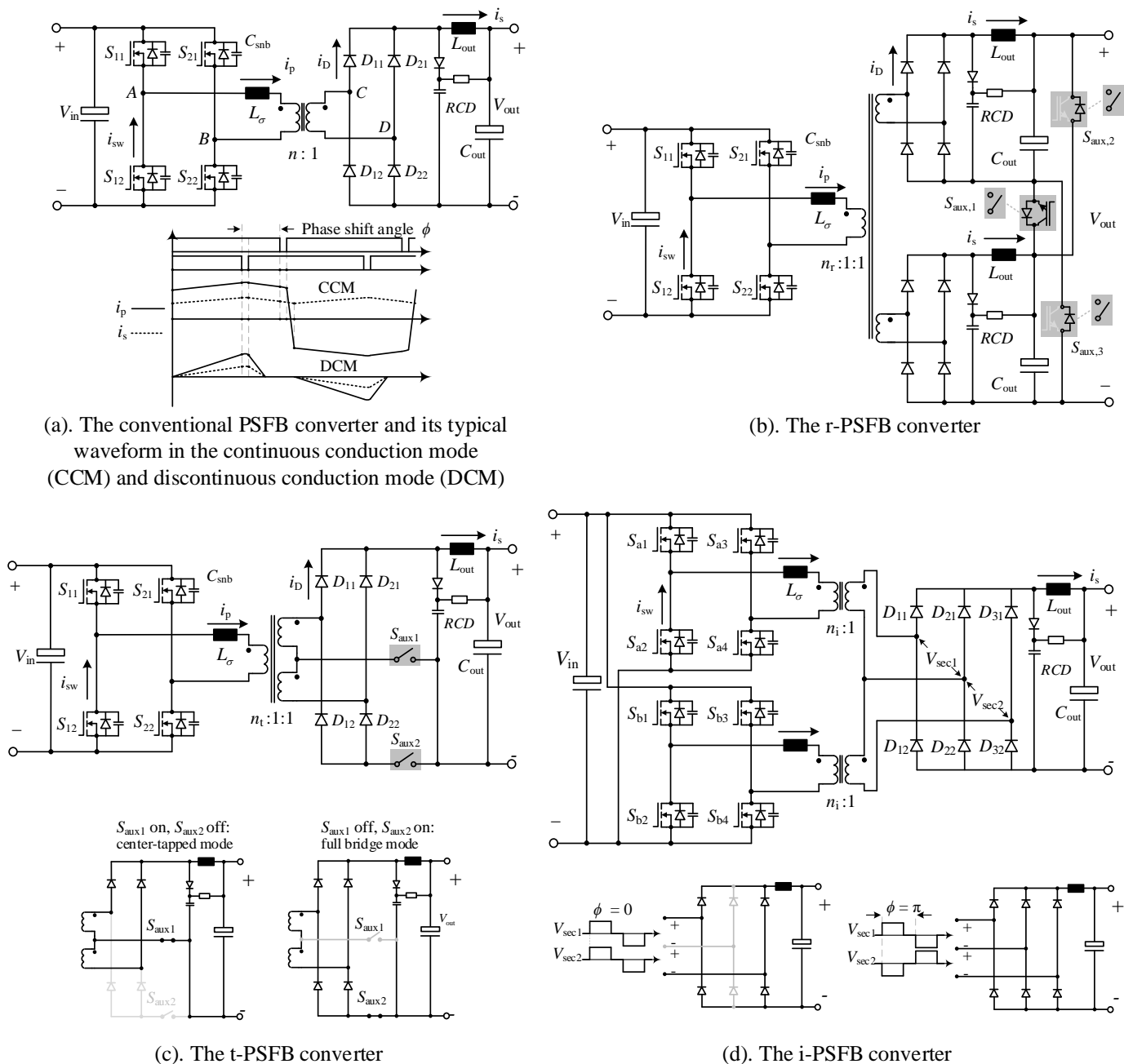


Fig. 1: The schematics of the conventional PSFB converter and three modified PSFB converters

voltage range is also halved.

Instead of using two diode rectifiers with the two-secondary-winding transformer like the r-PSFB converter, one single diode rectifier can be used together with two additional auxiliary switches to make a re-configurable PSFB converter, as shown in Figure 1(c). This converter, which is first introduced in the literature by this paper, is denoted here as the t-PSFB converter. The two-secondary-winding transformer and diode bridge of the t-PSFB converter can be configured into a full-bridge mode or a center-tapped mode by the connection of the auxiliary switches. Similar to the r-PSFB circuit, this t-PSFB converter reduces the operational phase shift control angle for the wide voltage operation. The number of rectifier diodes

needed is half compared to the r-PSFB circuit, but higher voltage rating rectifier diodes are required simultaneously.

In the study of Wu et al. [21], an LLC resonant converter with a hybrid rectifier is proposed. This LLC converter has two H-bridge inverters on the primary side, two transformers, and a three-leg diode bridge rectifier. By controlling the phase shift of the PWM signals of the two H-bridge inverters, the LLC converter can be operated as if the two circuits are connected in series or parallel. With this idea, the PSFB converter can be modified into an interleaved PSFB converter with a hybrid rectifier as shown in Figure 1(d). This converter, denoted as the i-PSFB, has the same performance regarding the reduction of operational phase shift in a wide voltage range like the

r/t-PSFB converters but has doubled transistors counts and different transformer designs. 1700V rating diodes are required for the EV charging application aiming at an 800V class battery as load.

These converters shown in Figure 1 are well-suited for the wide voltage range public EV charging application due to their characteristic of re-configuration. However, the optimal design and benchmark of these converters in terms of the cost, power density, and efficiency performance have not been done. The cost estimation in the academic research of power electronics is challenging, primarily due to the poor availability of the components' cost data. In [22] component cost models of switched-mode power converters with an approximate rated power between 5 and 50 kW are derived. These models are useful for engineers as they can be incorporated into the converter design process, and they are also used in [23], [24]. These component cost models are largely dependent on variables related to physical component properties, making them not so straightforward to implement. Moreover, large database acquired from manufacturers is needed for a better fitting, which is not easily accessible.

This paper aims to identify which one of the three modified PSFB converters is the most advantageous in the wide voltage range EV charging application, considering an 11kW power rating, 30A maximum output current, 640-840V input voltage, and 250-1000V output voltage range. To do so, A multi-objective design and benchmark process is proposed, with the normalized cost, average efficiency, and power density of the magnetic components and heatsink being the objectives of interest. Firstly, the essential data of the components are collected from the easily accessible database of the re-distributors. The data includes the cost per commercial off-the-shelf (COTS) component, conduction resistance of the transistors and rectifier diodes ($R_{ds(on)}$ and $R_{D(on)}$), switching loss of the transistor ($E_{on/off}$), the capacitive charge of the rectifier diodes (Q_c), weight and volume of the magnetic cores (M_c and V_c). It is worth mentioning that the data needs to cover various current and voltage ratings to compare topologies using different component requirements. Secondly, the correlation of cost versus the performance indexes of the components such as $R_{ds(on)}$, $E_{on/off}$, $R_{D(on)}$, Q_c , M_c and V_c are established by processing the data with curve-fitting methods. Different from the physical properties based cost models used in [22]–[24], the correlations directly connect the cost information to the performance indexes of the components based on the open and accessible data, without having a model in between. Therefore, these correlations are more straightforward to implement. With the obtained correlations, a collection of the possible designs by sweeping through a range of $R_{ds(on)}$, $E_{on/off}$, $R_{D(on)}$, Q_c , M_c and V_c can be made. In this way, the designs are not limited by certain components choices and the correlations can be directly utilized by other designers without a components database. The normalized cost of the possible designs, including the cost of semiconductors, magnetic components, gate drivers, heatsinks, and PCB boards, can be calculated, as well as the power density of the magnetic components and heatsinks. Additionally, the average efficiency performance can be calculated based on

the components chosen using the analytical models of the converters. As a result, a design space is formed based on the possible designs. Finally, the advantageous converter design can be selected.

The contribution of this paper is as follows:

- 1) The design guideline of three re-configurable structure PSFB converters that are well-suited for the wide voltage range public EV charging application is elaborated. Among the three re-configurable structure PSFB converters, the t-PSFB converter that utilize two auxiliary switches with a three-winding transformer is a new PSFB converter topology that is first introduced in this paper.
- 2) A multi-objective converter design process that considers the normalized cost, power density of the magnetic components and heatsinks, and the average efficiency performance is introduced. The accessible components data from the well-known re-distributors is collected and processed to uncover the correlation between the cost and the performance factors of the components.
- 3) The multi-objective design and performance benchmark of the 11kW t/r/i-PSFB converter and conventional PSFB converter for the wide output voltage range (250-1000V) EV charging application is presented. This design benchmark is particularly important, because it identifies the i-PSFB and r-PSFB converters as the outstanding solutions for the future EV market.

This paper is arranged as follows. In Section II, the operation principles of the three modified PSFB converters are introduced. Section III presents a basic comparison of the three converters in the circuitry level. In Section IV, the open and accessible data from the well-known re-distributors is collected, based on which the correlations among the components' cost and performance indexes are calculated. In Section V, the multi-objective design process of the converters are introduced. The design space of the converters is formed based on the design process. The normalized cost, power density of the magnetic components and heatsinks, and the average efficiency performance of the converters designs are benchmarked and interpreted. At last, a close-to-Pareto-front 45kHz r-PSFB prototype converter is built to verify the design and benchmark results. The prototype's operational waveform, efficiency performance, cost, and power density information are also presented. The conclusion of the work is presented in Section VII.

II. OPERATION PRINCIPLES OF THE RE-CONFIGURABLE PSFB CONVERTERS

A. The Conventional PSFB Converter

The conventional PSFB converter, as shown in Figure 1(a), consists of an H-bridge inverter, a high-frequency isolation transformer with an equivalent leakage inductance L_σ referred to the primary-side and a diode-bridge rectifier on the secondary side, and a second-order low-pass output passive filter consisting of L_{out} and C_{out} . Note that the diode-bridge rectifier are sometimes replaced by a synchronous rectifier using unipolar transistors to reduce conduction losses. The

optional lossless turn-off snubber capacitors C_{snb} at the full-bridge are for reducing turn-off switching losses (but it will narrow the ZVS turn-on range), and a voltage clamping RCD snubber circuit is used at the secondary-side between the terminal C and D for limiting the voltage spikes on the secondary side diodes [25].

The PSFB converter is typically controlled with fixed switching frequency by phase-shift modulation where the two half-bridge legs are operated with 50% duty cycle, as shown in the typical waveform depicted in Figure 1(a). The phase-shift angle Φ refers to the asynchronization between the operation of the two half-bridge legs. When Φ is null, the diagonal pair of transistors (S_{11} & S_{22} , or S_{12} & S_{21}) turn on and off synchronously, making the primary side voltage v_{AB} alternate between $+V_{in}$ and $-V_{in}$, which is equivalent to a bipolar modulation of the H-bridge inverter. When the Φ is non-null, the synchronization is broken, and the parallel pair of transistors (S_{11} & S_{21} , S_{12} & S_{22}) are able to be kept turned on at the same time, creating a third circuit state that is $v_{AB} = 0V$, leading to a controllable unipolar modulation action. Due to the impressed i_p caused by L_σ and inverter bridge capacitance, the switching transition in each half-bridge leg creates a lowered di_p/dt and dv_{AB}/dt on the primary side, making the ZVS turn-on possible and lowering the turn-off losses of the transistors. A complete description of the operation of a PSFB converter can be found in [26].

B. The r-PSFB Converter with Re-configurable Secondary Side

Figure 1(b) shows the schematic of the r-PSFB converter [12]. Three-winding transformer is used, with the turns ratio of $n_r : 1 : 1$. The primary side is identical to that of the conventional PSFB converter. Each of the secondary sides is connected to a diode-bridge rectifier, an output filter (L_{out} and C_{out}), and an RCD snubber circuitry. Three auxiliary switches $S_{aux,1,2,3}$ connect the two secondary sides and enable two different configurations according to their switching states. The auxiliary switches can be implemented by either mechanical switches or semiconductor transistors.

The re-configuration of the r-PSFB converter operates as follows. When $S_{aux,1}$ is kept on and $S_{aux,2,3}$ are kept off, the two diode rectifiers are connected in series, making V_{out} twice the individual diode rectifier output voltage. When $S_{aux,2,3}$ are kept on and $S_{aux,1}$ is kept off, the two diode rectifiers are connected in parallel. As a result, V_{out} equals the individual diode rectifier output voltage, but the output current is shared by the two rectifiers.

C. The t-PSFB Converter with Re-configurable Secondary Side

Figure 1(c) shows the schematic of the t-PSFB converter. A three-winding transformer is used, which has one primary and two secondary windings, with the turns ratio of $n_t : 1 : 1$. The primary side is identical to that of the conventional PSFB converter. The additional secondary winding and auxiliary switches ($S_{aux,1,2}$) allow the secondary side to be configured

into a regular full-bridge diode rectifier or a center-tapped diode rectifier.

The re-configuration of the t-PSFB converter operates as follows. When S_{aux1} is kept off and S_{aux2} is kept on, the two secondary windings are in series, and the t-PSFB works the same as a conventional PSFB converter with full-bridge diode rectifier. When S_{aux1} is kept on and S_{aux2} is kept off, the secondary side is configured into a center-tapped rectifier. This is shown in Figure 1(c).

D. The i-PSFB Converter with Hybrid Diode Rectifiers

Figure 1(d) shows the schematic of the i-PSFB converter. Two H-bridge inverters fed by V_{in} are connected in parallel on the primary side, and they can be interleaved. A hybrid three-legs diode rectifier is connected to the two H-bridge inverters by two transformers with the turns ratio of $n_i : 1$. Note that instead of parallel connecting the H-bridge inverters as shown in Figure 1(d), these could be alternatively connected in series, for instance, when connected to a bipolar dc grid.

The interleaving of the i-PSFB converter operates as follows. The two H-bridge inverters operate the same as that of the conventional PSFB converter, with an interleaving phase shift ϕ between them. When $\phi = 0$, the upper-side transformer secondary side voltage V_{sec1} is in phase with the lower-side V_{sec2} , resulting in the series connection of the two transformers' secondary windings. In this series connection mode, the first and third diode bridge-legs ($D_{11,12}$ & $D_{31,32}$) process all the current, and rectify the sum of V_{sec1} and V_{sec2} , while the second diode bridge-leg ($D_{21,22}$) is placed in off-state. When $\phi = \pi$, V_{sec1} and V_{sec2} are in reverse polarity, resulting in the parallel connection of the two transformer's secondary windings, which is facilitated by the added diode bridge-leg as shown in Figure 1(d). In this parallel connection mode, the first and third diode bridge legs are in parallel and share the inductor impressed current equally, while the second diode bridge leg processes the whole inductor current. Therefore, for even power loss balance in the rectifying stage, the diodes $D_{21,22}$ could be assembled with the hard paralleling of two diodes of the same technology used in the bridge legs containing $D_{11,12}$ and $D_{31,32}$.

III. CIRCUIT LEVEL COMPARISON AMONG CONVENTIONAL PSFB, R-PSFB, T-PSFB AND I-PSFB CONVERTERS

TABLE I: The equivalent parameters of the t,r,i-PSFB converters

conv-PSFB	t-PSFB		r-PSFB		i-PSFB	
	series	parallel	series	parallel	series	parallel
n_{eff}	$n/2$	n	$n/2$	n	$n/2$	n
$L_{out(eff)}$	L_{out}	L_{out}	$2L_{out}$	$L_{out}/2$	L_{out}	L_{out}
$C_{out(eff)}$	C_{out}	C_{out}	$C_{out}/2$	$2C_{out}$	C_{out}	C_{out}
$i_{D(eff)}$	i_D	i_D	i_D	$2i_D$	i_D	i_D
$i_{s(eff)}$	i_s	i_s	i_s	$2i_s$	i_s	i_s
$i_{sw(eff)}$	i_{sw}	i_{sw}	i_{sw}	i_{sw}	$i_{sw}/2$	$i_{sw}/2$

A general comparison of the components used among the conventional PSFB, r-PSFB, and i-PSFB converters are

conducted. The comparison parameters include the component count and the voltage and current stresses of the components. With these parameters, the cost and losses can be calculated for these converters for a primary evaluation.

A. Transformer Turns Ratios n

The transformer's turns ratio n of the conventional PSFB converter can be determined with:

$$n = kV_{in(min)}/V_{out(max)} \quad (1)$$

where k is a tuning factor used to compensate for the voltage drop across the circuit components and also to give a margin for the feedback control dynamics. Practically, k is typically set between $k=0.85 \dots 0.95$.

For the t-PSFB, r-PSFB, and i-PSFB converters, the transformer's turns ratios ($n_{t,r,i}$) are doubled compared to n , since the secondary sides of these converters can operate in modes where the two secondary windings are connected in series.

B. Output Filter L_{out} and C_{out}

The output filter L_{out} and C_{out} can be determined by a maximum allowed current and voltage ripple stress across the converter.

1) *Output Inductance L_{out}* : For the conventional PSFB converter, the peak-to-peak output current ripple $I_{out,ripple}$ across L_{out} in the continuous conduction mode (CCM) operation can be calculated by:

$$I_{out,ripple} = \frac{V_{in}D(1-D)}{2nL_{out}f_{sw}} \quad (2)$$

The maximum output inductor ripple ($I_{out,ripple(max)}$) happens when $D = 0.5$ and $V_{in} = V_{in(max)}$. Thus, $L_{out(min)}$ could be calculated as:

$$L_{out} \geq L_{out(min)} = \frac{V_{in(max)}}{8nI_{out,ripple(max)}f_{sw}} \quad (3)$$

For the t-PSFB converter, the minimum output inductance $L_{out(min),t}$ equals the $L_{out(min)}$ calculated in Equation (3), in order to satisfy the current ripple requirement in both the full-bridge and center-tapped modes. $I_{out,ripple(max)}$ for the t-PSFB converter happens when it is in the full-bridge mode, $D = 0.5$, and $V_{in} = V_{in(max)}$. When the t-PSFB converter is in the center-tapped mode, the worst-case current ripple equals $0.5I_{out,ripple(max)}$.

For the r-PSFB converter, the minimum output inductance $L_{out(min),r}$ equals the $L_{out(min)}$ calculated in Equation (3), in order to satisfy the current ripple requirement in both the series and parallel connection modes. $I_{out,ripple(max)}$ happens when the r-PSFB is in the parallel connection mode, and in the series connection mode, the worst-case output current ripple is only $0.5I_{out,ripple(max)}$.

For the i-PSFB converter, the minimum output inductance $L_{out(min),i}$ equals the $L_{out(min)}$ calculated in Equation (3), in order to satisfy the current ripple requirement in both the series and parallel connection modes. Therefore, the worst case current ripple in the series connection mode is $I_{out,ripple(max)}$, while in the parallel connection mode is $0.5I_{out,ripple(max)}$.

2) *Output Capacitance C_{out}* : For the conventional PSFB converter, the peak-to-peak output voltage ripple $V_{out,ripple}$ on C_{out} in CCM can be determined by:

$$V_{out,ripple} = \frac{I_{out,ripple}}{16f_{sw}C_{out}} \quad (4)$$

The maximum voltage ripple ($V_{out,ripple(max)}$) happens at $I_{out,ripple(max)}$. Thus, $C_{out(min)}$ can be calculated as:

$$C_{out} \geq C_{out(min)} = \frac{I_{out,ripple(max)}}{16f_{sw}V_{out,ripple(max)}} \quad (5)$$

For the t-PSFB converter, the minimum output capacitance value equals $C_{out(min)}$ calculated in Equation (5). $V_{out,ripple(max)}$ for the t-PSFB converter happens when the converter is in the full bridge mode, and the worst voltage ripple that can happen in the center-tapped mode is $0.5V_{out,ripple(max)}$. For the r-PSFB converter, the minimum output capacitance value equals $C_{out(min)}$ calculated in Equation (5). $V_{out,ripple(max)}$ for the r-PSFB converter happens when it is in the series connection mode, and in the parallel connection mode, the worst voltage ripple is $0.5V_{out,ripple(max)}$. For the i-PSFB converter, the minimum output capacitance value equals $C_{out(min)}$ calculated in Equation (5).

These information are summarized in Table II.

C. Voltage Stress of C_{out} and Current Stress of L_{out}

The voltage stress of C_{out} is the same for the conventional PSFB, t-PSFB, and i-PSFB converters, as the output capacitor in these converters needs to withstand the full output voltage V_{out} . However, for the r-PSFB converter, each of the output capacitors only needs to block $0.5V_{out}$.

The current stress of L_{out} depends on how the voltage, current, and power rating of the converter is set. Figure 2 shows the operation range of the converter. If the power rating is equal to or higher than P_1 , which allows the maximum output current value to be reached in the series connection mode, i.e., $P_1 = \frac{1}{2}V_{out(max)}I_{out(max)}$, then, the current stresses on L_{out} is identical for all four converters, because in the series connection mode all of the inductors of the four converters need to conduct the whole output current i_s plus the current ripple. If the power rating is smaller than P_2 , which means the maximum output current that can be reached during the series connection mode is $0.5I_{out(max)}$ (i.e., $P_2 = \frac{1}{2}V_{out(max)}\frac{1}{2}I_{out(max)}$), then the current stresses on the inductors of r-PSFB converter will be half of the other PSFB converter or even less. This information is summarized in Table II.

D. Voltage Stress of the RCD Snubber Circuitry

Due to the resonance between L_σ and the parasitic capacitance from the transformer and rectifier diodes, a voltage ringing will happen on the secondary side diodes, with a peak voltage value that could reach twice the nominal value of the secondary winding voltage [25] [12]. This can be critical for the safe operation of the rectifier diodes, and it is particularly critical for the voltage class (V_{class}) requirement of the fast-recovery diodes. Therefore, the RCD voltage clamp snubber circuitry is designed to limit the blocking voltage ringing to a

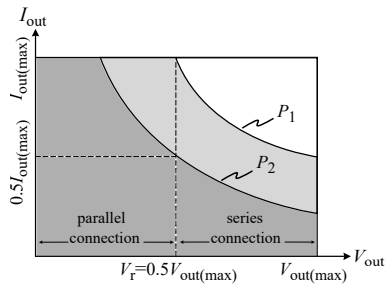


Fig. 2: Operation range of the converters and the power limitation

TABLE II: The summary of the components requirements for the four studied PSFB converters

	items	conv-PSFB	t-PSFB	r-PSFB	i-PSFB
transformer	turns ratio rated to n	1	2	2	2
output filter	L_{out} count	1	1	2×1	1
	C_{out} count	1	1	2×1	1
	V_{stress} of C_{out} rated to V_{out}	1	1	0.5	1
	I_{stress} of L_{out} rated to i_s	1	1	0.5 - 1	1
RCD	V_{stress} of D, C_{RCD} rated to V_{cp}	1	1	0.5	1
D_{rec}	V_{stress} of D_{rec} rated to V_{sec}	1	1	0.5	1

reasonable value, V_{cp} , so that a safe operation for the rectifier diodes is ensured, e.g., $V_{cp} \leq 0.85V_{class}$.

The voltage stress of the D_{RCD} and C_{RCD} equals to V_{cp} for the conventional PSFB converter, which could reach $2V_{sec}$ if no clamp snubber circuit is used. For the t-PSFB and i-PSFB converters, the voltage stress of the D_{RCD} and C_{RCD} equals to V_{cp} as well, since its series connection mode is equivalent to the conventional PSFB converter. For the r-PSFB converter, the RCD circuitry only needs to block half of the voltage compared to the conventional PSFB converter. However, the trade-off is that it has two sets of RCD circuitry. This information is summarized in Table II. The sizing of the resistance value and the power loss calculation of the RCD snubber follows the methodology explained in [12].

E. Voltage and Current Stresses of the Rectifier Diodes and Transistors

The voltage class of the rectifier diode of the PSFB converter needs to be paired with the V_{cp} of the RCD circuitry. Therefore, for the r-PSFB converter, the voltage class of the rectifier diode is halved compared to the other analyzed PSFB converters. This information is summarized in Table II.

After designing the transformer turns ratio and output filter as introduced in the previous subsections A and B, the steady-state current stresses of the rectifier diodes and transistors

TABLE III: The worst-case current stresses of the 11kW, 30A converters

	conv-PSFB	t-PSFB	r-PSFB	i-PSFB
$I_{p,rms}$ [A]	48.9	36.1	34.3	18
$I_{sw,rms}$ [A]	34.6	25.5	24.3	12.8
$I_{D,rms}$ [A]	21.1	21.2	14.8	21.2
$I_{D,avg}$ [A]	15	15	10.5	15

of the t,r,i-PSFB, and the conventional PSFB converter can be calculated using the steady-state analytical model of the PSFB converter introduced in [12] together with the equivalent parameters of the t,r,i-PSFB converters shown in Table I. Considering an 11kW power rating, 30A maximum output current, 640-840V input voltage, and 250-1000V output voltage range, the current stresses are summarized in Table III. As it can be seen from Table III, the worst-case $I_{p/sw,rms}$ of the t-PSFB and r-PSFB is lower than that of the conv-PSFB converter, and those of the i-PSFB converter is approximately half of those of the t-PSFB and r-PSFB. This is because the re-configuration ability of the t/r/i-PSFB converter can reduce the current stresses to the minimum half of those of the conv-PSFB converter if the power rating is chosen to be P_2 shown in Figure 2. However, since the chosen power rating of the benchmark study is 11kW, it lays between P_2 and P_1 . Thus, the current stress of t/r/i-PSFB converter is lower than the conv-PSFB but not as low as half, as in the case shown in Table III.

IV. KEY COMPONENTS DATA COLLECTION AND PROCESSING

In order to better evaluate the performance of the PSFB converters with different circuit component requirements, data of the necessary components are obtained from the website of the well-known re-distributors, and they are further processed using a python script to obtain the correlation among the parameters regarding efficiency performance, power density, and cost as shown in Figure 10. Using this approach, it is no longer necessary to extract the essential data from the datasheets of components, which is highly time-consuming. And since this method is purely based on data analysis and interpretation, physical models for cost estimation is not required. Other designers can incorporate the method to process their own components database, or they can directly use the numerical coefficients presented in this paper for a primary estimation in their design stage.

The unit price per piece from the re-distributors' website is used as the cost data of the components. This data is valuable for two reasons. Firstly, it is the most accessible price data. Mass production price information is usually only available from company quote or specific supply-chain. Thus, it is hard to access especially for the academic researchers and engineers in small-scale companies. Each company will also have different mass production price based on the size of the enterprise and their negotiation power. However, for prototyping or small-scale production, the price information provided online by these re-distributors is extremely valuable for the primary estimation of the cost. Secondly, the normalized price calculated based on the price per piece is similar to the one calculated using the price for large purchase quantities. To demonstrate this idea, the price information of 12 SiC MOSFETs in the package of TO-247 from three different manufacturers, GeneSiC, Infineon, and Wolfspeed are collected from the website of the re-distributor Digikey. The part number and the price information are shown in Table IV, where $price_1$ stands for the unit price if the purchase quantity

is 1, price_{1000} means the unit price if buying 1000 pieces, etc. Plotting the unit price of different purchase quantities in Figure 3, one can see that the unit price for larger purchase quantities drops considerably. However, instead of the exact price, this paper emphasis on predicting the normalized cost of design, i.e., how much cheaper or more expensive is one certain converter design compared to the others. By calculating the pu value of the prices for different purchase quantities, Figure 4 shows that the normalized cost calculated using different purchase quantities remains similar. Thus, the easy-to-access unit price information from the well-known redistributors enables the estimation of the relative price of the converter designs, which is insightful for the academic researchers and small-scale company engineers to make design decisions. Moreover, this price information can still be used with a scaling factor by the companies to predict the mass production price.

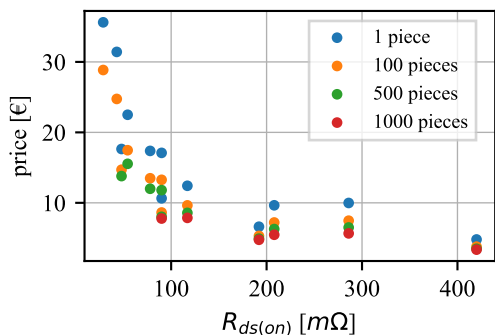


Fig. 3: The unit price of the SiC MOSFETs in Euros. Data collected on 3rd, Jan, 2023.

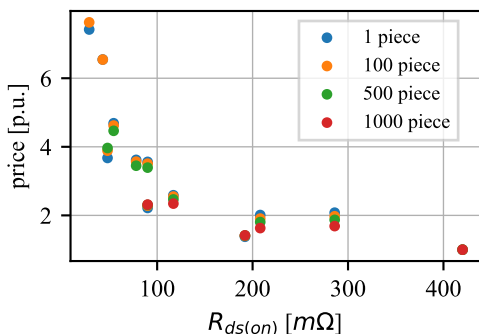


Fig. 4: The unit price of the SiC MOSFETs in pu values. Data collected on 3rd, Jan, 2023.

A. Active Semiconductors

For SiC MOSFETs, the on-state (static) losses can be determined by their on-resistance R_{dson} and the switching (or dynamic) losses can be modelled by the accumulative energy dissipated during the on/off switching transition ($E_{\text{on/off}}$). Their cost data can be collected directly on the website of their redistributors, e.g., Digikey website. In this work, only semiconductor devices employing TO-247 packaging are considered

in the analysis. Several SiC MOSFET manufacturers are evaluated, and a statistic curve-fitting method is used to model the important parameters for the calculation of the selected design performance metrics.

Figure 5 shows the correlation between the R_{dson} and cost of the transistors with three voltage class devices, and Table V shows the curve-fitting numerical parameters of the plotted logarithmic equation. It can be seen that with the same R_{dson} , the SiC MOSFETs with higher voltage ratings generally cost more. At low R_{dson} , the cost difference between the 1700V, 1200V, and 650V classes is more significant. This may imply that circuits designed for a given target efficiency that employ 1700V semiconductors could have higher costs than the ones employing 1200V or 650V devices, but one should be careful because the total cost of a power electronic converter is highly dependent on the circuit topology selection and the complexity of the circuit. It is interesting to note that there are fewer options for the 1700V semiconductor market when compared to the 650V and 1200V classes. This indicates that topologies using 1700V SiC transistors will be more prone to supply chain problems.

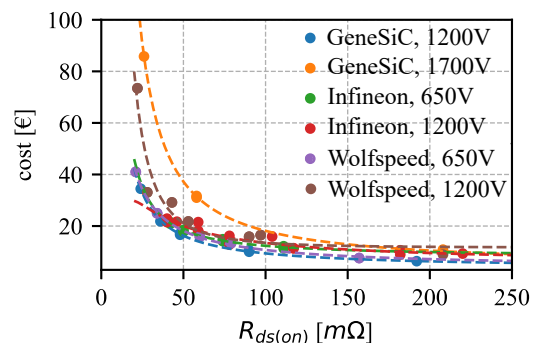


Fig. 5: SiC MOSFET price and $R_{\text{ds(on)}}$ trend, depending on the device voltage ratings. The plotted dots are the data of a commercially available device acquired from the Digikey website on 2022-02-22, containing SiC MOSFET from 'GeneSiC', 'Infineon', 'Wolfspeed'. The device package is limited to TO-247. The dashed lines are the obtained curve-fitting correlations, whose method and coefficients are shown in Table V.

The correlation between switching losses $E_{\text{on/off}}$ and R_{dson} of several commercially available 1200V SiC MOSFETs from Wolfspeed is given in Figure 6. Herein, the data considers the device datasheet information: $E_{\text{on/off}}$ at 800V, 30A, 25°C of junction temperature, 5Ω external gate resistance, and a 15V/-5V gate driving voltage. Table VI shows the numerical coefficients of the curve-fitting first-order linear equation.

It is worth mentioning that the data collected from the datasheet is under the specific conditions of 800V and 30A. Therefore, the $E_{\text{on/off}}$ for other operating points can be scaled proportionally based on the actual blocking voltage and switching current, as shown in Equation (6).

$$E_{\text{on/off}}(t) = \frac{V_{\text{block}}(t)}{800V} \cdot \frac{I_{\text{sw}}(t)}{30A} E_{\text{on/off}}(\text{fit}) \quad (6)$$

TABLE IV: Price of SiC MOSFETs for different purchase quantities collected on 3rd, Jan, 2023.

part_num	mfr	$R_{ds(on)}$ [mΩ]	price ₁ [€]	price ₁₀ [€]	price ₁₀₀ [€]	price ₅₀₀ [€]	price ₁₀₀₀ [€]
G3R350MT12D	GeneSiC	420.0	4.80	4.261	3.7815	3.47872	3.35618
G3R160MT12D	GeneSiC	192.0	6.61	5.921	5.3067	4.91578	4.75678
G3R75MT12D	GeneSiC	90.0	10.64	9.580	8.6284	8.01880	7.77066
G3R40MT12D	GeneSiC	48.0	17.64	16.102	14.7000	13.79436	NaN
IMW120R220M1H	Infineon	286.0	9.98	9.019	7.4672	6.50228	5.66326
IMW120R090M1H	Infineon	117.0	12.42	11.414	9.6395	8.57498	7.86534
IMZ120R060M1H	Infineon	78.0	17.37	15.969	13.4866	11.99730	NaN
IMW120R040M1H	Infineon	54.4	22.50	20.682	17.4668	15.53798	NaN
C3M0160120D	Wolfspeed	208.0	9.65	8.709	7.2106	6.27890	5.46872
C3M0075120D	Wolfspeed	90.0	17.09	15.711	13.2688	11.80356	NaN
C3M0032120D	Wolfspeed	43.0	31.42	28.979	24.7468	NaN	NaN
C3M0021120D	Wolfspeed	28.8	35.62	33.229	28.8516	NaN	NaN

TABLE V: Curve fitting method and coefficients for the relation between price and $R_{ds(on)}$ of the SiC MOSFETs, depending on the manufacturers and voltage ratings. Data only include those with $R_{ds(on)} < 300m\Omega$.

fitting method	$cost_T = a \cdot (1/R_{ds(on)})^2 + b \cdot (1/R_{ds(on)}) + c$					
Mfr	Infineon	Infineon	GeneSiC	GeneSiC	Wolfspeed	Wolfspeed
V_{rating} [V]	650	1200	1200	1700	650	1200
a	7.91e+03	-8.33e+03	4.71e+03	2.53e+04	2.15e+03	2.99e+04
b	3.66e+02	9.08e+02	5.44e+02	1.15e+03	6.78e+02	-1.34e+02
c	7.89e+00	5.21e+00	3.47e+00	4.10e+00	3.72e+00	1.19e+01

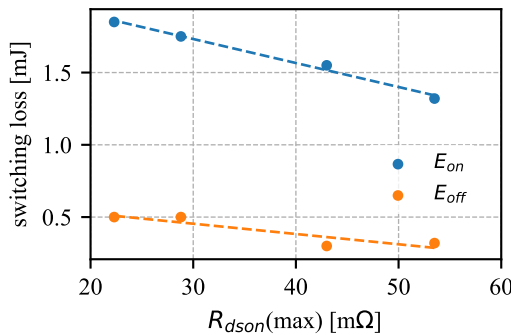


Fig. 6: SiC MOSFET $E_{on/off}$ and $R_{ds(on)}$ trend. The dots are the data acquired from the datasheets of 1200V SiC MOSFET from 'Wolfspeed', the condition is at 800V, 30A, 25°C of junction temperature, 5Ω gate resistance, and 15V/-5V gate driving voltage. The package is limited to TO-247. The dashed lines are the curve-fitting correlations, whose method and coefficients are shown in Table VI.

TABLE VI: Curve fitting method and coefficients for the relation between $E_{on/off}$ and $R_{ds(on)}$ of the 1200V SiC MOSFETs. Data includes those from 'Wolfspeed'.

fitting method	$E_{on/off} = a \cdot R_{ds(on)} + b$	
parameter	E_{on}	E_{off}
a	-1.66e-02	-7.11e-03
b	2.23e+00	6.67e-01

TABLE VII: Curve fitting method and coefficients for the relation between price and $R_{D(on)}$ of the SiC diodes, depending on the manufacturers and voltage ratings.

fitting method	$cost_D = a \cdot (1/R_{D(on)})^2 + b \cdot (1/R_{D(on)}) + c$				
Mfr	Infineon	Infineon	GeneSiC	GeneSiC	Wolfspeed
V_{rating} [V]	650	1200	1200	1700	1200
a	-4.34e+02	-2.72e+02	-4.98e+03	1.11e+02	-6.17e+03
b	2.47e+02	2.97e+02	7.48e+02	5.29e+02	6.78e+02
c	3.23e+00	2.55e+00	-3.96e+00	2.30e+00	5.61e+00

B. SiC rectifier diodes

Discrete TO-247 SiC diodes from various manufacturers from 650V to 1700V are compared using the information provided on their datasheets. The conduction loss of the diodes is typically calculated by Equation (7), where $R_{D(on)}$ and V_D are the on resistance and forward voltage drop. The $R_{D(on)}$ is taken from the on-state IV-curve of the device by the difference in voltage drop for two reference current values, e.g., one at half-rated current and another at full-rated current. V_D is the voltage drop value taken when the device conducts only a tiny fraction of the rated current.

$$P_D = I_{D,rms}^2 \cdot R_{D(on)} + I_{D,avg} \cdot V_D \quad (7)$$

Figure 7 and table VII shows the correlation between price and $R_{D(on)}$ of the rectifier diodes, grouped by the device voltage class. Note that since the SiC diodes benchmarked are of the same technology, their equivalent constant voltage drop V_D are similar and closely independent of the chip die area (or rated current of the device). Therefore, the $R_{D(on)}$ parameter has a more logical relationship with the chip die size (or current ratings) and thus relates better with the device cost.

The switching loss of the diodes is typically calculated by Equation (8), where Q_c is the capacitive charge of the diodes. Figure 8 show the correlation between the $R_{D(on)}$ and Q_c .

$$P_{D(sw)} = 0.5 \cdot Q_c \cdot V_D \cdot f_{sw} \quad (8)$$

C. Magnetic core material and Litz Wire

Magnetic components account for a significant part of the cost, loss, and power density of a power electronic converter. The magnetic core loss is generally calculated by iGSE

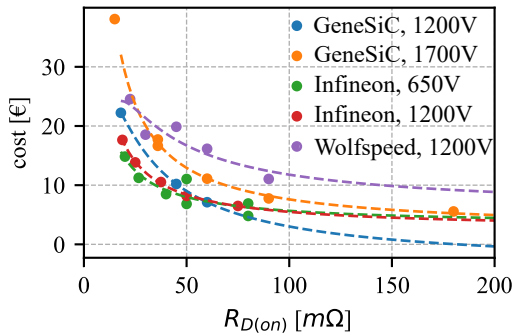


Fig. 7: SiC rectifier diode price and $R_{D(on)}$ trend. The dots are the data acquired from Digikey on 2022-02-22, containing SiC diodes from 'GeneSiC', 'Infineon' IDW series, and 'Wolfspeed'. The package is limited to TO-247. The dashed lines are the curve fitting trends of the SiC rectifier diodes, whose method and coefficients are shown in Table VII.

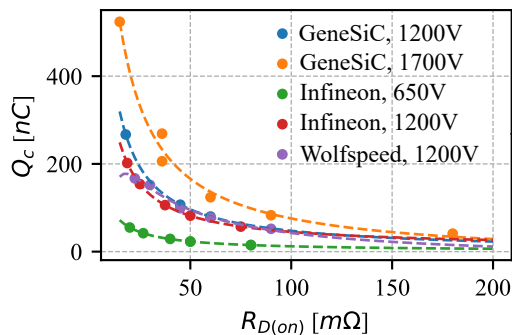


Fig. 8: SiC rectifier diode Q_c and $R_{D(on)}$ trend. The dots contain SiC diodes from 'GeneSiC', 'Infineon' IDW series, and 'Wolfspeed'. The package is limited to TO-247. The dashed lines are the curve fitting trends of the SiC rectifier diodes, whose method and coefficients are shown in Table VIII.

for non-sinusoidal excitation, which requires the Steinmetz coefficients measured for sinusoidal excitation that need to be curve-fitted based on the datasheet figures. The cost of the magnetic cores for various core shapes can be obtained through suppliers' websites, such as Digikey, and the trend of the core cost and core mass is shown in Figure 9. It can be seen that the core cost has a linear correlation with the amount of core material used. Table IX shows the curve-fitting coefficients of the magnetic cores.

TABLE VIII: Curve fitting method and coefficients for the relation between Q_c and $R_{D(on)}$ of the SiC diodes, depending on the manufacturers and voltage ratings.

fitting method	$Q_c = a \cdot (1/R_{D(on)})^2 + b \cdot (1/R_{D(on)}) + c$				
Mfr	Infineon	Infineon	GeneSiC	GeneSiC	Wolfspeed
V_{rating} [V]	650	1200	1200	1700	1200
a	-1.19e+03	-1.52e+03	-1.54e+03	-2.38e+04	-6.40e+04
b	1.14e+03	3.72e+03	4.92e+03	9.75e+03	7.17e+03
c	8.33e-01	7.90e+00	-1.57e+00	-1.95e+01	-2.27e+01

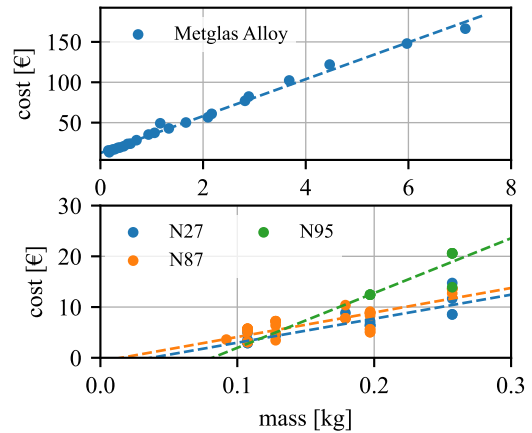


Fig. 9: Magnetic core trend. The dots are the data acquired from Digikey on 2022-02-21, containing E shaped cores for the ferrite material N27, N87, N95, and U shaped AMCC cores for Metglas Alloy material.

TABLE IX: Curve fitting method and coefficients of the magnetic cores

fitting method	$cost_c = a \cdot M_c + b$			
material	Metglas Alloy	N27	N87	N95
a	22.85	47.31	48.29	107.97
b	12.39	-1.76	-0.73	-8.83

For the Litz wire used in the magnetic components, €5.38 per kilogram is used to estimate the cost of it based on the amount of copper used. The weight of the copper can be calculated based on the number of turns and the mean-length-per-turn of the design.

D. Heatsink

The heatsink is necessary for the thermal management of the semiconductors used in the studied PSFB converters. Therefore, its size will be mostly defined by the critical point in which the system can be placed into operation where the semiconductor losses are maximum. Independently on the performance of the heatsink, its minimal size will be defined by the sum of surface area required to accommodate each used TO-247 packaged device. The thermal resistance of the heatsink depends on the material used, available surface area, airflow, and equivalent pressure drop. For simplicity of comparison, only the aluminum heatsinks that are rectangular in shape with the same fin height and arrangement from the same manufacturer HS marston are considered. Table X shows the details of the chosen heatsinks. Due to the excellent performance of the selected heatsinks, the needed surface area for placing the semiconductors of each studied circuit topology defines their required size.

E. Gate driver, relay and PCB

The high-side gate driver ISO5852 is considered in the benchmark study. The price per unit is €7. For the conv/t/PSFB converter, four gate drivers are required. And for the i-

TABLE X: The details of the heatsinks considered for the four converters. The price information is collected from Farnell on 2022/10/24.

topology	heatsink	SA[m ²]	volume[L]	cost[€]
conv/t-PSFB	890SP-01000-A-100	0.010	0.325	50.87
r-PSFB	890SP-01500-A-100	0.015	0.488	67.87
i-PSFB	890SP-02000-A-100	0.020	0.650	79.70

PSFB converter, eight are required. For the digital controller, the Texas Instruments TMS320F28379D is considered. The price is €27. The relays used in the r/t-PSFB converter is chosen to be the T9GV1L14-5, which is a 30A power relay with a unit price of €7.4 and a conduction resistance of about 10mΩ. These prices are based on the data from mouser/Farnell website acquired on 2022/10/24.

The price of the PCB board depends mainly on the number of conductive layers and the size of the board. Assuming that 1m² of the standard 4 layers 1 ounce copper PCB is used, and that the size of the PCB equals the size of the heatsink, the price of the single PCB boards for the four converters are estimated to be €8.5 for the conv/t-PSFB, €13.1 for the r-PSFB and €17.4 for the i-PSFB. This price was obtained from the manufacturer Eurocircuits on 2022/10/24.

V. MULTI-OBJECTIVE DESIGN OF THE CONVERTERS

To benchmark the four studied PSFB topologies in the EV battery charging application, a multi-objective design process is performed in all circuits while considering an 11kW power rating, 30A maximum output current, 640-840V input voltage, and 250-1000V output voltage range. For the EV charging application where the converter operates in a wide output voltage range and mostly in full-power/current, the averaged full-power/current efficiency η_{AVG} is used as the indicator of the system efficiency performance instead of the efficiency value for a single operational point. η_{AVG} is the average value of the steady-state efficiencies of a certain number of sampling operational points. These sampling operational points starts from the minimum output voltage and maximum output current to the maximum output voltage and maximum power, with a constant output voltage increment between two neighboring points. In this paper, eight points are considered for the calculation. The first point is when $V_{out} = 300V$ and $I_{out} = 30A$, the second is $V_{out} = 400V$ and $P = 11kW$, the third is $V_{out} = 500V$ and $P = 11kW$, etc., and the final point is when $V_{out} = 1000V$ and $P = 11kW$. The objectives of interest are the average efficiency performance, power density of the magnetic components and heatsinks, and normalized cost. Figure 10 shows the flowchart of the multi-objective design process.

The first step of the multi-objective design process is to design the magnetic components of the converters. Since the switching frequency f_{sw} of the converter has a significant impact on the design of the magnetic components, the magnetic components are designed for f_{sw} from 15kHz to 105kHz, and assuming the worst case scenario in terms of losses. The design spaces of the magnetic components will be formed for

each of the converters, with the loss, power density, and cost being the figure of merit. Then, based on the design spaces, some advantageous transformer and inductor designs will be selected for further converter design.

The second step is to sweep through a range of $R_{ds(on)}$ and $R_{D(on)}$. Using the components correlation derived and the analytical models of the converters, the total cost and the average efficiency of the converter designs can be calculated. The calculated total costs can be further processed to obtain the normalized costs by taking the minimum value of the cost as 1. By using the normalized costs, the designs with the cost advantage can be identified, while the error of cost estimation brought by the changing market price can be reduced at the same time. As a result, the design spaces for the converters can be formed, and the advantageous converter topology and component designs can be chosen.

A. Magnetic Components Designs

The design of the magnetic components follows the process illustrated in Figure 10. In order to avoid overly large number of solutions, the Litz wire considered in the design is set to be AWG 41 and 600 strands, the core material for the transformer is the ferrite N87, for the inductor is the Metglas Amorphous Cut Core, and the core shape for the transformer is the EE cores, and for the inductor are the UU cores. Five design variables are considered for finding the optimal design, they are the switching frequency, the core size, number of stacked cores, flux density, and the number of litz wires that can be put in parallel. The number of stacked cores can change from 1 to 8 for transformer design, and 1 to 5 for inductor design. The allowed flux density is from 10% to 80% of the B_{sat} of the core material. The number of litz wires that can be paralleled can be 1 or 2 for the ease of winding assembling. The worst-case scenarios for the designs of the magnetic components happen when the winding currents are the maximum, which results in the most losses. For the transformer design, the worst-case scenario for conv-PSFB converter is when $V_{in} = 840V$, $I_{out} = 30A$, $V_{out} = 366V$, and for the t/r/i-PSFB converter is when $V_{in} = 840V$, $I_{out} = 22A$, $V_{out} = 500V$. For the inductor design, the worst-case scenario for r-PSFB converter is when $V_{in} = 840V$, $I_{out} = 22A$, $V_{out} = 366V$, and for the conv/t/i-PSFB converter is when $V_{in} = 840V$, $I_{out} = 30A$, $V_{out} = 366V$. The loss calculation is conducted using the method from [27]. Combining the total losses P_{mag} (W) and surface area A_{mag} (m²) of the magnetic components, the temperature rise ΔT is estimated based on Equation (9) [28].

$$\Delta T = \left(\frac{P_{mag}}{10 \cdot A_{mag}} \right)^{0.833} \quad (9)$$

This temperature rise estimation equation is obtained by lumping the winding losses together with the core losses and assume that the thermal energy is dissipated uniformly throughout the surface area of the core and winding assembly at all ambient temperatures. This assumption is effective, because the majority of the transformer's surface area is ferrite core area rather than winding area, and the thermal conductivity of ferrite (around 40 mW/cm²/°C) is poor at any

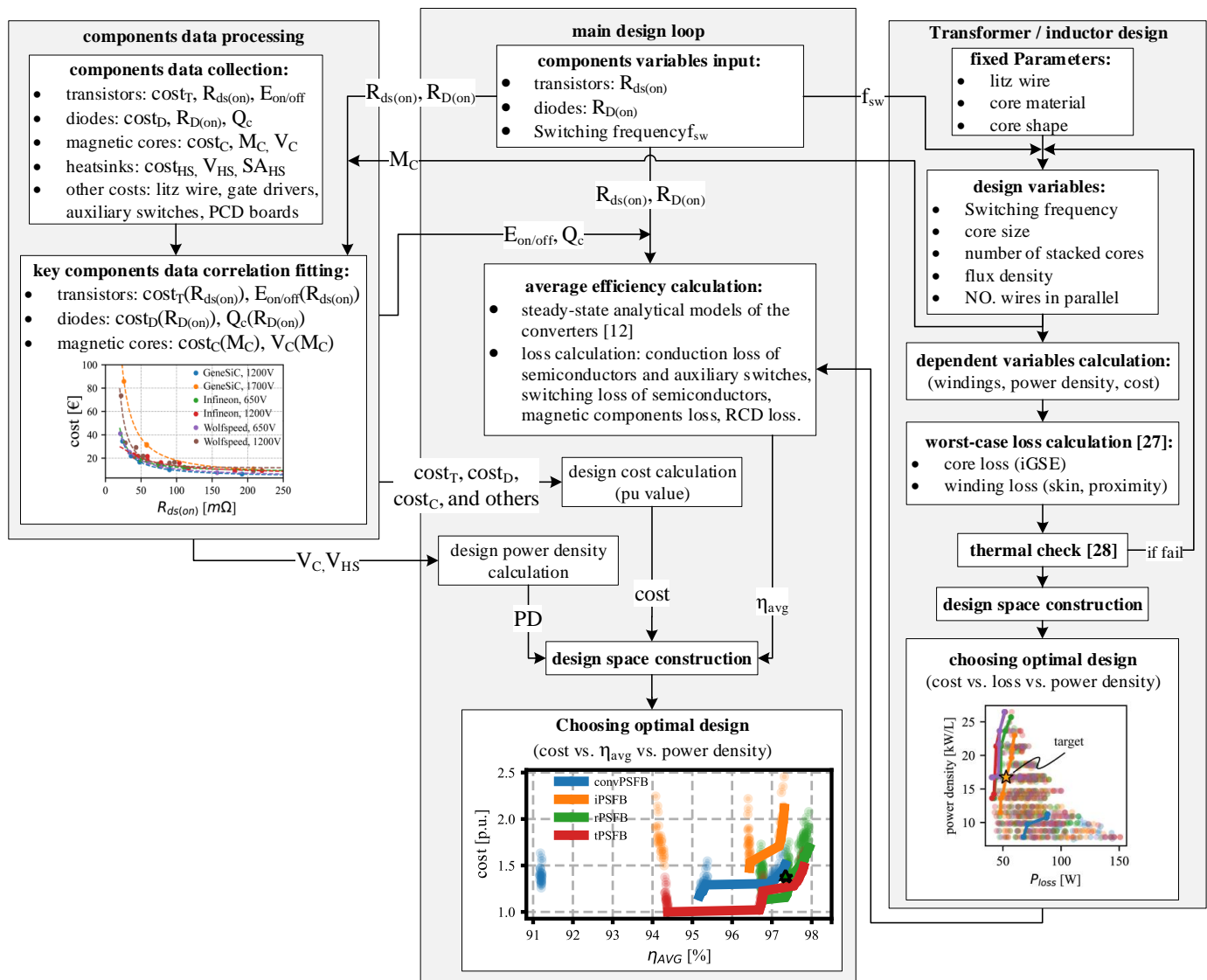


Fig. 10: The multi-objective design process of the converters

temperature. And since the transformer uses several pairs of ferrite core stack together, the magnetic cores are carefully fix together so that the airgap is uniformed in the whole transformer. In this way, the magnetic flux and thus core loss can be more evenly distributed among the cores, which helps avoid creating hotspot. Moreover, the windings are tightly winded on the bobbin, and the gaps among the wires are kept as uniformly as possible, so that the winding losses are also distributed evenly in the winding area.

Figure 11 shows the worst-case transformer loss P_{loss} and the power density values of the transformer designs for all four topologies, with the switching frequency changing from 15kHz to 135kHz. It can be seen that by increasing f_{sw} from 15kHz to 75kHz, P_{loss} decreases and power density increases for all of the topologies. However, there is no apparent improvement on P_{loss} and power density anymore when f_{sw} further increase above 75kHz.

The underlining reason is that, by increasing f_{sw} , less number of turns is needed for the transformer to operate with

the desired value of magnetic flux density B . As a result, a smaller winding area, which naturally means a smaller core shape, is needed to make a transformer with a higher f_{sw} . The reduced winding length and core size further contribute to the reduction of core loss. However, there is a limit to how small the transformer can become with the increase of f_{sw} , which is mostly regulated by the thermal management performance of the component. One can argue that a smaller flux density B should be used for the transformer with higher f_{sw} so that the loss-per-volume of the core does not result in overheating. Unfortunately, a smaller flux density can only be achieved with an increased number of turns, which, again, calls for a larger winding area, as well as a larger core size. In summary, there is an optimal f_{sw} , with which the transformer design yields the advantageous P_{loss} and power density without having an overheating problem. From Figure 11, it is clear that the optimal f_{sw} for the transformer designs is around 75kHz.

Based on the results shown in Figure 11, three advantageous transformer designs that have the highest power density and

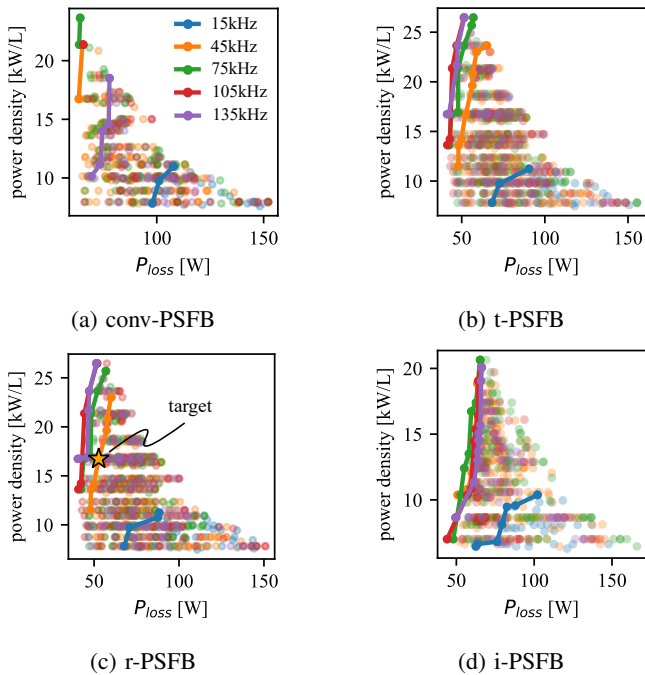


Fig. 11: The transformer designs for the four PSFB topologies at $f_{sw} = 15, 45, 75, 105, 135\text{kHz}$. The design constrains are: target transformer leakage inductance $L_{\sigma}=10\mu\text{H}$ (referred to the primary side), N87 as core material, winding layer arrangement is limited to first primary, then secondary 1 and secondary 2 side-by-side, calculated temperature rising limited to 80°C .

lowest power losses at f_{sw} of 15kHz, 45kHz, and 75kHz are collected for each one of the PSFB topologies. Table XI shows the chosen transformer designs. It can be seen from Figure 11 and Table XI that the transformer designs of the t-PSFB and r-PSFB is able to have lower power losses when compared to the conv-PSFB and i-PSFB. This is because the winding current stresses of these two topologies are less, as can be seen from Table III. And despite having two transformers, The total cost of the transformers of the i-PSFB converter can be even cheaper than the other three PSFB converters in 15kHz and 45kHz. However, due to the added winding volume of the two transformers, the total power density of the transformers are slightly lower than the other three options.

Figure 12 shows the worst-case loss and power density values of the inductor designs for all four PSFB topologies, with the f_{sw} in the range from 15kHz to 135kHz. Note that here f_{sw} is defined as the MOSFET switching frequency, therefore in any of the studied PSFB, the equivalent frequency seen by the inductor will be twice f_{sw} . It can be seen that, similar to the transformer design, the inductor designs have their optimal f_{sw} for achieving the optimal loss and power density values. The conv-PSFB converter has the best inductor design at $f_{sw} = 15\text{kHz}$, and with higher f_{sw} , the loss increases and power density decreases. For the t/r/i-PSFB converters, the optimal inductor designs occurs around $f_{sw} = 45\text{kHz}$. This is because the inductor of the conv-PSFB converter suffers from higher dB/dt stress compared to the other re-configurable

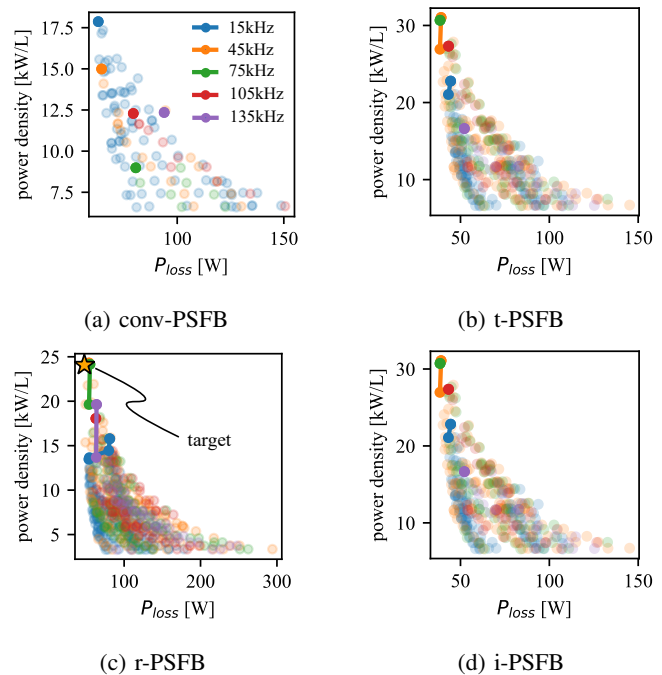


Fig. 12: The inductor designs for the four PSFB topologies at $f_{sw} = 15, 45, 75, 105, 135\text{kHz}$. The design constrains are: Metglas as core material, maximum temperature rising lower than 80°C . Note that here f_{sw} is defined as the MOSFET switching frequency, therefore in any of the studied PSFB the equivalent frequency seeing by the inductor will be twice f_{sw} .

structure PSFB converters despite the current stresses on the inductors for the conv/t/i-PSFB are the same. This results in increased core loss on the inductor according the iGSE equation [27].

Table XII shows the selected inductor designs that have the optimal loss and power density values for f_{sw} of 15kHz, 45kHz, and 75kHz for all topologies. It can be seen based on Figure 12 and Table XII that the inductor designs of the conv-PSFB converter performs worse in terms of power losses, due to the high dB/dt stress explained before. In comparison, the t-PSFB and i-PSFB have similar inductor designs that are the most advantageous in terms of power losses, power density, and cost. For the r-PSFB converter, the total power density of the two inductors is less, and the total power losses are higher than that of the t-PSFB and i-PSFB. This is reasonable since the chosen power rating of 11kW and output current limitation of 30A makes the r-PSFB design right in between P_1 and P_2 in Figure 2. This makes the worst-case current stress on each the inductors of the r-PSFB converter to be less than that of the conv/t/i-PSFB converter, but also more than half of it. Therefore, the two inductors of the r-PSFB together has higher losses in the worst case, and lower power density.

B. Multi-Objective Design Results

With the magnetic components at different f_{sw} designed, the performance of these converters in different f_{sw} can be benchmarked. A range of $R_{ds(on)}$ and $R_{D(on)}$ are swept through.

TABLE XI: Detailed information of the transformer designs that are chosen for the multi-objective design process. The P_{loss} , Power Density (PD), and cost are calculated for all the transformers.

topology	f_{sw} [kHz]	P_{loss} [W]	PD [kW/L]	cost [€]	ΔT [°C]	shape [E core]	N_{core}	$N_{\text{w,prim}}$	$N_{\text{w,sec}}$	N_{prim}	N_{sec}	B_{op} [T]
convPSFB	15.0	107.8	11.0	123.4	78.4	E 70/33/32	5	2	2	12	19	0.248
convPSFB	45.0	65.2	21.4	66.3	73.0	E 56/24/19	8	2	2	5	8	0.248
convPSFB	75.0	64.1	23.6	58.2	78.8	E 56/24/19	7	2	2	5	9	0.155
tPSFB	15.0	90.5	11.2	122.5	69.2	E 70/33/32	5	2	1	12	10	0.248
tPSFB	45.0	56.4	19.6	56.4	72.5	E 65/32/27	3	2	2	10	8	0.217
tPSFB	75.0	52.6	21.7	49.2	77.7	E 70/33/32	2	2	2	8	7	0.186
rPSFB	15.0	88.3	11.2	122.5	67.8	E 70/33/32	5	2	1	12	10	0.248
rPSFB	45.0	57.4	19.6	56.4	73.5	E 65/32/27	3	2	2	10	8	0.217
rPSFB	75.0	53.2	21.7	49.2	78.6	E 70/33/32	2	2	2	8	7	0.186
iPSFB	15.0	102.1	10.4	99.1	72.9	E 70/33/32	2	1	1	31	25	0.248
iPSFB	45.0	71.7	18.7	40.9	76.3	E 55/28/21	2	1	2	22	18	0.217
iPSFB	75.0	65.3	20.6	50.1	74.8	E 56/24/19	3	1	2	10	9	0.186

TABLE XII: Detailed information of the inductor designs that are chosen for the multi-objective design process. The P_{loss} , Power Density (PD), and cost are calculated for all the inductors.

topology	f_{sw} [kHz]	P_{loss} [W]	PD [kW/L]	cost [€]	ΔT [°C]	shape [U core]	N_{core}	$N_{\text{w,prim}}$	N_{prim}	B_{op} [T]
convPSFB	15.0	63.0	17.9	86.6	79.7	U AMCC-25	4	2	42	0.936
convPSFB	45.0	64.5	15.0	99.5	67.5	U AMCC-40	4	2	21	0.468
convPSFB	75.0	80.6	9.0	136.5	60.0	U AMCC-80	4	2	14	0.312
tPSFB	15.0	44.4	22.8	65.0	70.8	U AMCC-25	3	2	42	1.248
tPSFB	45.0	39.1	31.0	43.1	79.1	U AMCC-25	2	2	29	0.936
tPSFB	75.0	38.5	30.7	43.0	78.1	U AMCC-25	2	2	27	0.624
rPSFB	15.0	53.8	13.5	87.7	54.4	U AMCC-25	2	2	49	1.248
rPSFB	45.0	48.0	24.1	44.1	70.8	U AMCC-25	1	2	45	0.936
rPSFB	75.0	55.2	24.2	43.6	79.6	U AMCC-25	1	2	34	0.780
iPSFB	15.0	44.4	22.8	65.0	70.8	U AMCC-25	3	2	42	1.248
iPSFB	45.0	39.1	31.1	43.1	79.1	U AMCC-25	2	2	29	0.936
iPSFB	75.0	38.5	30.7	43.0	78.1	U AMCC-25	2	2	27	0.624

And based on the cost and performance correlations of the key components and information about miscellaneous parts obtained in Section IV, the relative cost and losses of every design can be estimated for the different choice of components. Then combined with the magnetic components and the RCD snubber circuit, the system efficiency performance can be estimated using the analytical models of the converters. The detailed analytical model of the PSFB type converter used in this paper is presented in [12].

Figure 13 shows η_{AVG} and the relative cost of all the possible designs. First of all, it can be seen from Figures 13a and 13b that by increasing the switching frequency, the cost will drop, and the power density of the magnetics will increase. However, η_{AVG} will also drop. This trade-off mainly comes from the reduction of magnetic components material and the increase of switching loss of the semiconductors when increasing f_{sw} . At 15kHz, the optimal design can be obtained from the t-PSFB converter. When f_{sw} increases to 45kHz, the designs of the r-PSFB converter start to be competitive since the power density increases and cost reduces considerably while η_{AVG} suffers less reduction compared to the other topologies. When f_{sw} further increases to 75kHz, the gain on the power density increase and cost saving is limited, while η_{AVG} drops significantly for the conv/t/i-PSFB converters.

Secondly, in terms of the power density of the magnetic components and heatsinks and normalized price of the converters, the t-PSFB converter is able to deliver the lowest cost and highest power density designs from 15kHz to 75kHz. Even though the conv-PSFB has the same components count as the t-PSFB, the current stress of the transformer and the dV/dt stress of the inductor of the t-PSFB is less than that of the conv-PSFB due to the feature of re-configuration. This factor benefits the t-PSFB converter to have more power efficient, smaller, and cheaper designs of magnetic components. The i-PSFB converter is the most expensive one due to the high component account. The r-PSFB converter which has 8 rectifier diodes with 1200V voltage ratings is slightly more expensive than the t-PSFB which has 4 rectifier diodes with 1700V voltage rating. This corresponds to the trend shown in Figure 5 that the cost of the 1200V rectifier diodes are less expensive than the 1700V ones with the same $R_{\text{D(on)}}$, but not less than half.

Thirdly, in terms of η_{AVG} , the i-PSFB and r-PSFB topology is able to provide the η_{AVG} -advantageous designs in 15kHz. The conv-PSFB generally has lower η_{AVG} , especially when f_{sw} increases. To better interpret the η_{AVG} performance of these converters, two designs of each converter topology that have the highest η_{AVG} and lowest normalized cost in 15kHz

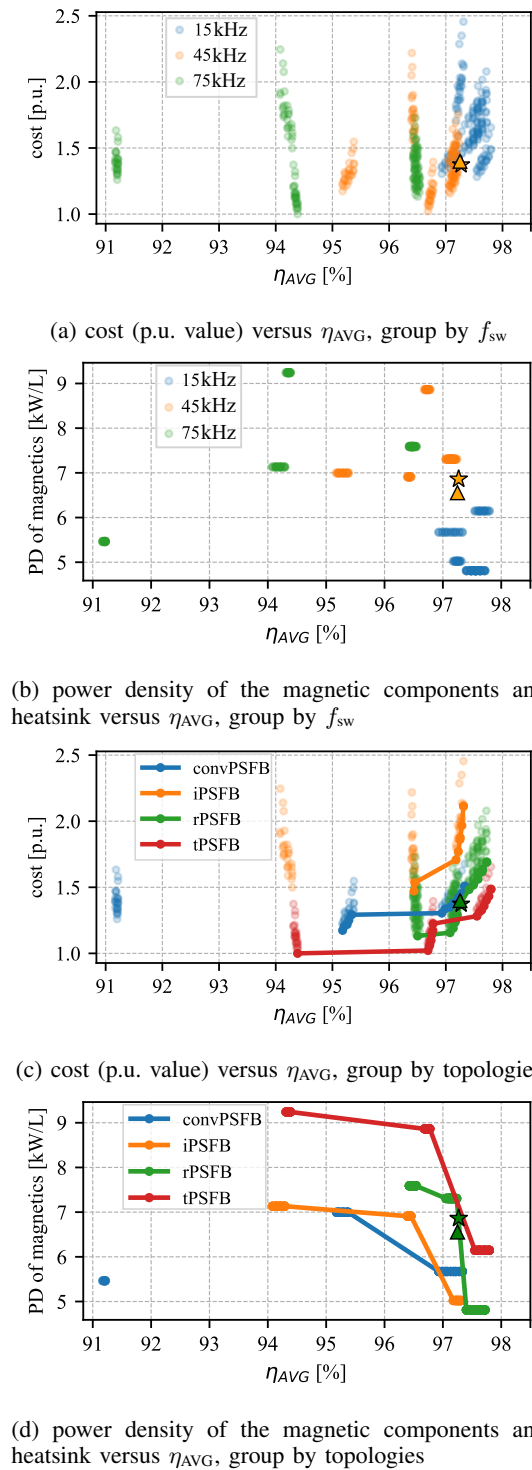


Fig. 13: The averaged full-power/current efficiency (η_{AVG}), the cost, and the power density of the magnetic components and heatsink of the possible designs of all four PSFB topologies. The target design and the actual prototype design are marked as the star and triangle respectively.

and 45kHz are selected for further analysis. The detailed information about these designs are summarized in Table XIII, and the breakdown of the averaged losses of these designs are illustrated in Figure 14.

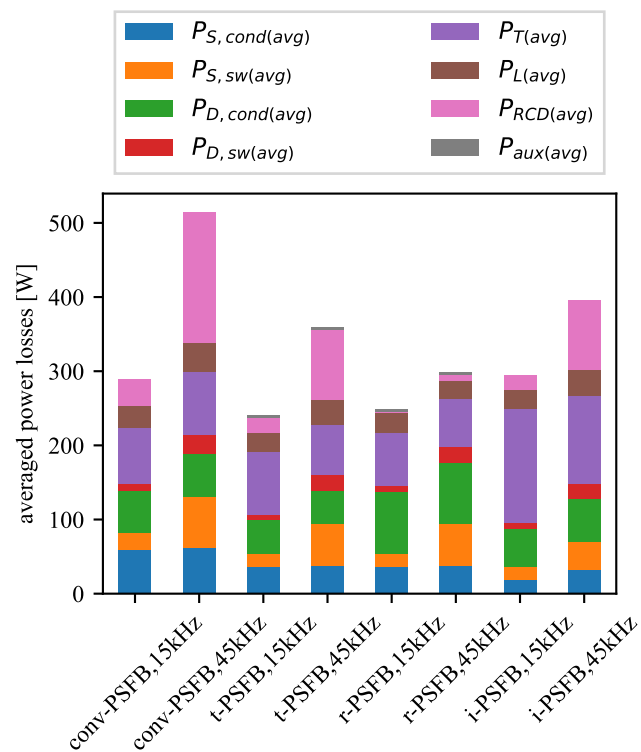


Fig. 14: The breakdown of the averaged losses of the advantageous designs from Figure 13. $P_{S,cond(avg)}$ and $P_{D,cond(avg)}$ are the averaged conduction loss on the transistors and rectifier diodes, $P_{S,sw(avg)}$ and $P_{D,sw(avg)}$ are the averaged switching loss on the transistors and rectifier diodes, $P_{T(avg)}$ and $P_{L(avg)}$ are the averaged transformer losses and inductor losses, $P_{RCD(avg)}$ is the averaged RCD snubber circuitry loss, $P_{aux(avg)}$ is the averaged auxiliary switch conduction losses.

From Figure 14 it can be seen that the averaged conduction loss and switching loss on the transistors of the t/r/i-PSFB designs are less than that of the conventional PSFB design. This is due to the re-configuration ability, the t/r/i-PSFB topologies are able to have less current stress on the transistors in the low output voltage operation. This point is also revealed in the worst-case current stresses listed in Table III. It is an interesting observation that the i-PSFB converter has the lowest transistor losses. The first reason is that the i-PSFB converter has shared current stresses on the two full-bridges, which potentially lowers the total conduction loss according to the resistive loss calculation $P_{Ohmic} = I^2R$. The second reason is that the use of transistors with relatively high $R_{ds(on)}$ brings less switching losses, as shown in Figure 6. The r-PSFB converter designs have higher losses on the rectifier diodes. This is mainly due to the doubled amount of diodes on the conduction path, and the current is shared only during the parallel-connection configuration when V_{out} is low. The i-PSFB converter designs have the highest transformer losses even though the current is shared between the two transformers. The main reason is that the dB/dt stress on the transformers are not shared. In terms of inductor losses, the r-PSFB converter performs better than the other three converter. By having

TABLE XIII: Detailed information of the efficiency and cost advantageous designs based on Figure 13. PD_T is the power density of the transformers, PD_L is the power density of the inductors, PD is the power density of the magnetic components together with the heatsinks.

topology	f_{sw} [kHz]	η_{AVG} [%]	cost[pu]	transistor[m Ω]	rec diode[m Ω]	PD_T [kW/L]	PD_L	PD
conv-PSFB	15	97.33	1.51	Infineon,30	GeneSiC, 30	11.0	17.9	5.67
conv-PSFB	45	95.38	1.38	Infineon, 30	GeneSiC, 30	21.4	15.0	7.00
t-PSFB	15	97.80	1.48	Infineon, 30	GeneSiC, 30	11.2	22.8	6.15
t-PSFB	45	96.78	1.22	Infineon, 30	GeneSiC, 30	19.6	31.0	8.86
r-PSFB	15	97.72	1.69	Infineon, 30	Infineon, 30	11.2	13.5	4.81
r-PSFB	45	97.24	1.36	Infineon, 30	Infineon, 30	19.6	24.1	7.31
i-PSFB	15	97.31	2.11	Infineon, 30	GeneSiC, 30	10.4	22.8	5.02
i-PSFB	45	96.45	1.53	GeneSiC, 50	GeneSiC, 40	18.7	31.1	6.91

two secondary sides, the dB/dt stress on the two inductors of the r-PSFB converter are halved in the series connection operation due to the voltage sharing, which helps reducing the averaged inductor core losses. The most significant difference in losses lays in the snubber circuitry loss $P_{RCD(avg)}$. The r-PSFB converter has significantly less $P_{RCD(avg)}$ compared to the others, while the conv-PSFB suffers the highest $P_{RCD(avg)}$. This can be explained by the equations used for calculating the resistance value and the power loss of the RCD snubber circuitry, whose details can be found in [25] [12]. Due to the split secondary sides, not only high resistance value can be used for the RCD snubber circuits of the r-PSFB converter, the voltage stress on the R_{RCD} is also much less compared to the other topology. In practical implementation, this splitting structure of r-PSFB topology also brings benefit of loss sharing on the two RCD circuitries, which means simpler thermal design as well.

Based on these observations of the multi-objective design results, the t-PSFB converter operating at 15kHz and the r-PSFB converter at 45kHz with the right choices of semiconductor components stands out as the most advantageous converter designs in terms of the normalized cost, power density of magnetics and heatsinks, and η_{AVG} performance.

VI. EXPERIMENTAL VERIFICATION

In order to verify the multi-objective design prediction, a close-to-Pareto-front 45kHz r-PSFB prototype converter is built based on the multi-objective optimization design process described previously. Due to the availability issue of the components in today's market, the prototype converter has to be built with some adjustments on the selection of components. The ferrite core shape used for the transformer design changes from the intended EE65/32/27 from Table XI to the EE70/33/32, since the prior was out of stock in our trusted suppliers. The MOSFETs and rectifier diodes used in the prototype are IMW120R030M1H and IDW30G120C5B from Infineon, which were immediately available in the laboratory of the authors. The inductors are designed according to the optimal inductor design in Table XII. Table XIV shows the detail parameters and components used for the prototype converter. As a result, the target design is marked as the star shown in Figure 13, which is close to the obtained Pareto front of the design space.

Figure 15 shows the picture of the 45kHz r-PSFB prototype converter. The prototype converter has a power density of

TABLE XIV: Specifications of the prototype

input voltage [V]	640-840
output voltage [V]	250-1000
power rating [kW]	11
f_{sw} [kHz]	45
MAX output current [A]	30
transistor	IMW120R030M1H
rectifier diode	IDW30G120C5B
transformer core material	N87
transformer core shape	3xEE70/33/32
transformer $N_{prim}: N_{sec}$	8:7
inductor design	refer to Table XII
gate driver	ISO5852
DSP controller	TMS320F28379D

2.68kW/L. Figures 16 and 17 show the operational waveform of the prototype in parallel and series connection mode with different V_{out} and I_{out} . Figure 18 shows the waveform of the RCD clamping circuitry of the r-PSFB prototype. It can be seen that the prototype converter is able to operate in an extensive output voltage range from 250V to 1000V with different output current conditions, and the voltage clamping circuitry functions well.

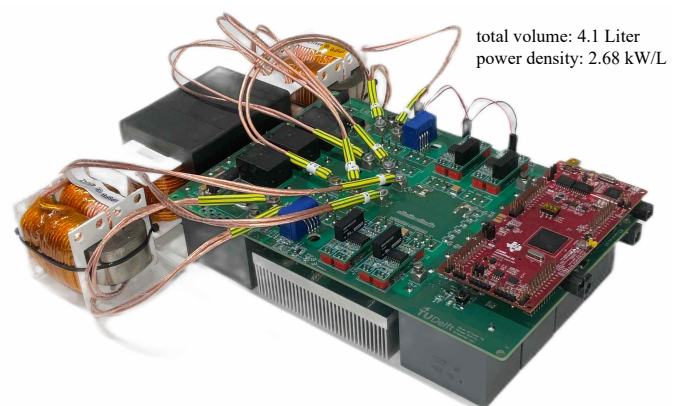


Fig. 15: Prototype of the 45kHz r-PSFB converter

In order to verify the efficiency performance of the 45kHz r-PSFB prototype converter, the full-power/current efficiency is tested and plotted together with the estimated efficiency in Figure 19. Additionally, the estimated efficiency of the optimal conv-PSFB converter design at 45kHz as listed in Table XIII is also plotted for comparison. It can be seen that

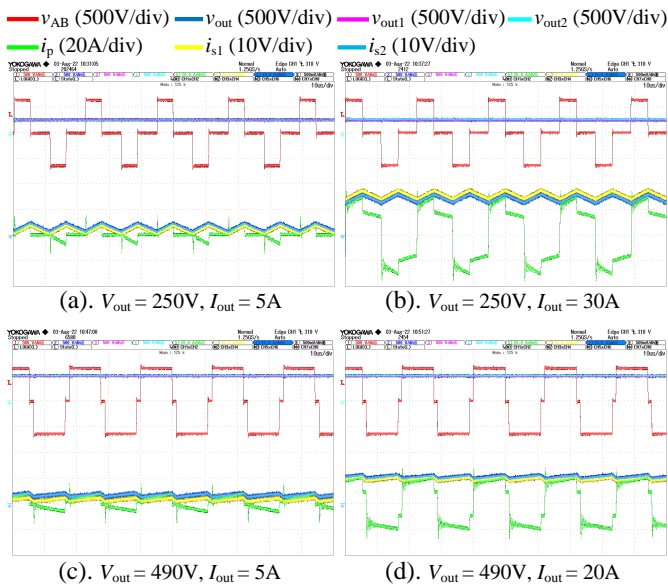


Fig. 16: The operational waveform of the r-PSFB converter in parallel connection mode, with $V_{in}=640V$. $v_{out1/2}$ and $i_{s1/2}$ are the output voltage and current of the two secondary side rectifiers, measured after the RCD circuitry and on the output inductors, respectively.

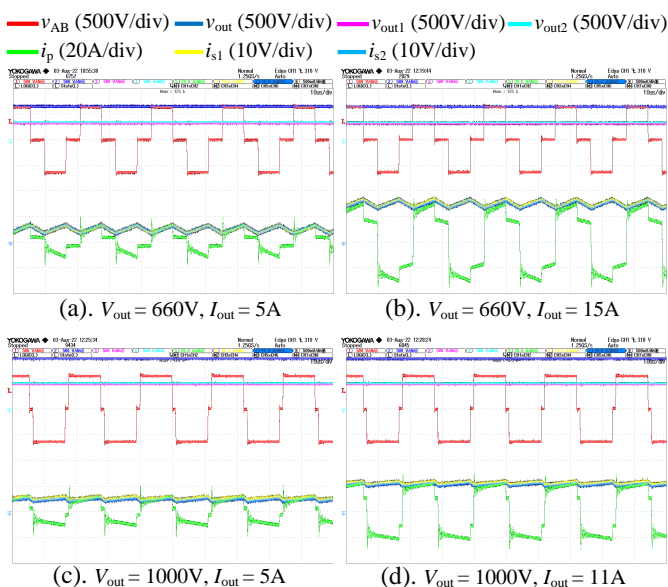


Fig. 17: The operational waveform of the r-PSFB converter in series connection mode, with $V_{in}=640V$.

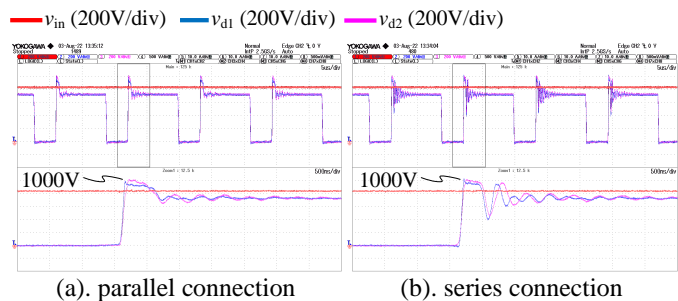


Fig. 18: The voltage clamping waveform of the RCD snubber circuitry, with $V_{in}=840V$. $v_{d1,2}$ are the diode voltage of the two secondary sides.

the test efficiency of the r-PSFB prototype matches well with the estimation. The peak efficiency achieved is 97.76%. The tested average full power/current efficiency is 97.25%, which is very close to the estimated value of 97.27%. The error in loss prediction is mainly due to the simplification of both analytical models for the conduction and switching losses of the semiconductors. The actual cost and average efficiency of the prototype are plotted in Figure 13 as the triangle, and it can be seen that the prototype implementation is very close to the target. The efficiency of the r-PSFB converter drops as V_{out} decreases from 1000V to 500V, due to the increasing phase shift angle and associated circulating losses. However, when V_{out} decreases further below 500V, the r-PSFB converter re-configures from series connection to parallel connection, resetting the phase shift angle and bringing up the efficiency. In comparison, the efficiency of the 45kHz optimal conv-PSFB design drops constantly as V_{out} decreases. This demonstrate the efficiency benefit of the re-configurable structure PSFB converters.

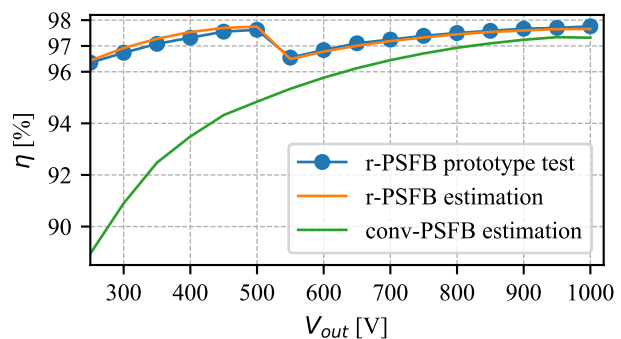


Fig. 19: The estimated efficiency of the 45kHz r-PSFB and conv-PSFB converter designs and the test efficiency of the 45kHz r-PSFB prototype converter with full power or maximum output current, $V_{in}=640V$.

VII. CONCLUSION

In this paper, three re-configurable structure PSFB converters are analyzed and benchmarked for the extended wide voltage range public EV charging application. A multi-objective converter design process that considers the normalized cost,

TABLE XV: Detailed information of the target r-PSFB design and the achieved r-PSFB prototype design from Figure 13

	f_{sw} [kHz]	η_{avg} [%]	cost [p.u.]	Magnetics&heatsink PD
target	45	97.27	1.37	6.86 [kW/L]
prototype	45	97.25	1.40	6.56 [kW/L]

power density of the magnetic components and heatsinks, and the average efficiency performance is introduced. In this proposed design process, well-accessible data provided by the components re-distributors are utilized to establish the correlations between the cost and loss performance of the components, which are used in the design process to determine the most advantageous converter in terms of the cost, power density of the magnetics and heatsink, and the averaged efficiency. Based on the resulted design space of the converters, A close-to-Pareto-front 45kHz r-PSFB prototype converter is built to verify the analysis, and the actual cost, power density of the magnetics and heatsink, and averaged efficiency match with the design well. This proves the feasibility of proposed multi-objective design and benchmark process, and identify the t-PSFB and r-PSFB converters to be the outstanding solutions in the wide voltage range public EV charging application.

REFERENCES

[1] D. Aggeler, F. Canales, H. Zelaya-De La Parra, A. Coccia, N. Butcher, and O. Apeldoorn, "Ultra-fast DC-charge infrastructures for EV-mobility and future smart grids," in *2010 IEEE PES Innovative Smart Grid Technologies Conference Europe (ISGT Europe)*, 2010-10, pp. 1–8.

[2] D. S. Gautam, F. Musavi, M. Edington, W. Eberle, and W. G. Dunford, "An automotive onboard 3.3-kW battery charger for PHEV application," *IEEE Transactions on Vehicular Technology*, vol. 61, no. 8, pp. 3466–3474, 2012-10.

[3] B. Gu, J.-S. Lai, N. Kees, and C. Zheng, "Hybrid-switching full-bridge DC–DC converter with minimal voltage stress of bridge rectifier, reduced circulating losses, and filter requirement for electric vehicle battery chargers," *IEEE Transactions on Power Electronics*, vol. 28, no. 3, pp. 1132–1144, 2013-03.

[4] T. Mishima, K. Akamatsu, and M. Nakaoka, "A high frequency-link secondary-side phase-shifted full-range soft-switching PWM DC–DC converter with ZCS active rectifier for EV battery chargers," *IEEE Transactions on Power Electronics*, vol. 28, no. 12, pp. 5758–5773, 2013-12.

[5] B. Whitaker, A. Barkley, Z. Cole, B. Passmore, D. Martin, T. R. McNutt, A. B. Lostetter, J. S. Lee, and K. Shiozaki, "A high-density, high-efficiency, isolated on-board vehicle battery charger utilizing silicon carbide power devices," *IEEE Transactions on Power Electronics*, vol. 29, no. 5, pp. 2606–2617, 2014-05.

[6] B. Whitaker, A. Barkley, Z. Cole, B. Passmore, T. McNutt, and A. B. Lostetter, "A high-frequency, high-efficiency silicon carbide based phase-shifted full-bridge converter as a core component for a high-density on-board vehicle battery charging system," in *2013 IEEE ECCE Asia Downunder*, 2013-06, pp. 1233–1239.

[7] W.-Y. Choi, M.-K. Yang, and H.-S. Cho, "High-frequency-link soft-switching PWM DC–DC converter for EV on-board battery chargers," *IEEE Transactions on Power Electronics*, vol. 29, no. 8, pp. 4136–4145, 2014-08.

[8] M.-K. Yang, H.-S. Cho, S.-J. Lee, and W.-Y. Choi, "High-efficiency low-cost soft-switching DC-DC converter for EV on-board battery chargers," in *2015 IEEE Applied Power Electronics Conference and Exposition (APEC)*, 2015-03, pp. 2050–2055.

[9] V. R. K. Kanamarlapudi, B. Wang, N. K. Kandasamy, and P. L. So, "A new ZVS full-bridge DC–DC converter for battery charging with reduced losses over full-load range," *IEEE Transactions on Industry Applications*, vol. 54, no. 1, pp. 571–579, 2018-01.

[10] M.-S. Lee, C.-Y. Lim, K.-W. Kim, M.-H. Park, and G.-W. Moon, "A phase-shift full-bridge converter with novel voltage oscillation clamping circuit for electric vehicle on-board charger," in *2019 10th International Conference on Power Electronics and ECCE Asia (ICPE 2019 - ECCE Asia)*, 2019-05, pp. 2040–2045.

[11] C. Lim, Y. Jeong, and G. Moon, "Phase-shifted full-bridge DC–DC converter with high efficiency and high power density using center-tapped clamp circuit for battery charging in electric vehicles," *IEEE Transactions on Power Electronics*, vol. 34, no. 11, pp. 10945–10959, 2019. [Online]. Available: <https://ieeexplore.ieee.org/document/8643533/>

[12] D. Lyu, T. B. Soeiro, and P. Bauer, "Design and implementation of a re-configurable phase-shift full-bridge converter for wide voltage range ev charging application," *IEEE Transactions on Transportation Electrification*, pp. 1–1, 2022.

[13] "porsche taycan models," Available at <https://www.porsche.com/international/models/taycan/taycan-models/taycan>.

[14] "IONIQ 5 brochure," Available at <https://www.hyundai.co.uk/brochures>.

[15] "Production ready rapide e given world debut at auto shanghai," Available at <https://www.astonmartin.com/en/our-world/news/2019/04/30/production-ready-rapide-e-given-world-debut-at-auto-shanghai>, 2019.

[16] "lucid air." [Online]. Available: <https://www.lucidmotors.com/air>

[17] J. Kolar, R. Wieser, and H. Ertl, "Analysis of a wide speed range starter/alternator system based on a novel converter topology for series/parallel stator winding configuration," in *Conference Record of the 1999 IEEE Industry Applications Conference. Thirty-Forth IAS Annual Meeting (Cat. No.99CH36370)*, vol. 4, 1999, pp. 2631–2641 vol.4.

[18] P. Sun, L. Zhou, and K. M. Smedley, "A reconfigurable structure DC–DC converter with wide output range and constant peak power," *IEEE Transactions on Power Electronics*, vol. 26, no. 10, pp. 2925–2935, 2011-10.

[19] M. A. Bakar and K. Bertilsson, "A modified higher operational duty phase shifted full bridge converter for reduced circulation current," *IEEE Open Journal of the Industrial Electronics Society*, vol. 1, pp. 82–96, 2020.

[20] M. A. Bakar, M. F. Alam, A. Majid, and K. Bertilsson, "Dual-mode stable performance phase-shifted full-bridge converter for wide-input and medium-power applications," *IEEE Transactions on Power Electronics*, vol. 36, no. 6, pp. 6375–6388, 2021-06.

[21] H. Wu, X. Zhan, and Y. Xing, "Interleaved llc resonant converter with hybrid rectifier and variable-frequency plus phase-shift control for wide output voltage range applications," *IEEE Transactions on Power Electronics*, vol. 32, no. 6, pp. 4246–4257, 2017.

[22] R. Burkart and J. W. Kolar, "Component cost models for multi-objective optimizations of switched-mode power converters," in *2013 IEEE Energy Conversion Congress and Exposition*, 2013, pp. 2139–2146.

[23] M. Stecca, C. Tan, J. Xu, T. B. Soeiro, P. Bauer, and P. Palensky, "Hybrid si/sic switch modulation with minimum sic mosfet conduction in grid connected voltage source converters," *IEEE Journal of Emerging and Selected Topics in Power Electronics*, vol. 10, no. 4, pp. 4275–4289, 2022.

[24] S. Waffler, M. Preindl, and J. W. Kolar, "Multi-objective optimization and comparative evaluation of si soft-switched and sic hard-switched automotive dc-dc converters," in *2009 35th Annual Conference of IEEE Industrial Electronics*, 2009, pp. 3814–3821.

[25] S.-Y. Lin and C.-L. Chen, "Analysis and design for red clamped snubber used in output rectifier of phase-shift full-bridge zvs converters," *IEEE Transactions on Industrial Electronics*, vol. 45, no. 2, pp. 358–359, 1998.

[26] U. Badstubner, "Ultra-High Performance Telecom DC-DC Converter," Ph.D. dissertation, ETH, Zurich, Apr. 2012. [Online]. Available: <https://www.pes-publications.ee.ethz.ch>

[27] J. Muhlethaler, "Modeling and Multi-objective Optimization of Inductive Power Components," Ph.D. dissertation, ETH, Zurich, Jan. 2012. [Online]. Available: <https://www.pes-publications.ee.ethz.ch>

[28] G. Orenchak, "Estimating temperature rise of transformers," vol. 30, pp. 14–22, 07 2004.